Title
Electronic and Polar Properties of Vanadate Compounds Stabilized by Epitaxial Strain

Journal
Chemistry of Materials, 30(17)

ISSN
0897-4756

Authors
Angsten, T
Martin, LW
Asta, M

Publication Date
2018-09-11

DOI
10.1021/acs.chemmater.8b01499

Peer reviewed

CHEMISTRY OF MATERIALS
Cite This: Chem. Mater. 2018, 30, 5870−5877
Article
pubs.acs.org/cm

Electronic and Polar Properties of Vanadate Compounds Stabilized by Epitaxial Strain

Thomas Angsten,*[,†] Lane W. Martin,[†,‡] and Mark Asta[†,‡]

[†]Department of Materials Science and Engineering, University of California, Berkeley, California 94720, United States
[‡]Materials Sciences Division, Lawrence Berkeley National Laboratory, Berkeley, California 94720, United States

Supporting Information

ABSTRACT: Recent experimental and computational studies have demonstrated pressure and epitaxial stabilization of polar $PbVO_3$ phases with perovskite-derivative crystal structures. In this study, we demonstrate, by density functional theory (DFT) calculations, the stability of similar perovskite-derivative structures in the KVO_3 and $NaVO_3$ systems when subjected to compressive biaxial strain. The electronic structure and polar properties of these compounds are computed as a function of biaxial strain, and the results are compared to those obtained for experimentally observed $PbVO_3$ structures. It is demonstrated that the substitution of Pb with monovalent K or Na cations increases the strength of the vanadyl bond due to the removal of the spatially extended Pb 6p states. Both KVO_3 and $NaVO_3$ exhibit epitaxially stabilized perovskite-derivative phases having large polarizations and only small total energy increases relative to their unstrained bulk structures. The calculated epitaxial phase diagram for KVO_3 predicts a strain-energy driving force for a phase separation from −4% to 1.5% misfit strain into a polar *Cm* phase, having square-pyramidal coordination of the *B*-site, and a paraelectric *Pbcm* phase, having tetrahedral coordination of the *B*-site. The results show that strain-stabilized polar vanadate compounds may occur for other compositions in addition to $PbVO_3$ and that changes in the *A*-site species can be used to tune bonding, structure, and functional properties in these systems.

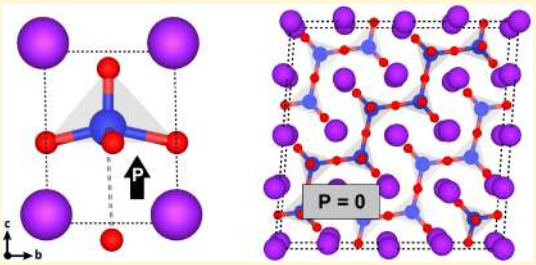

1. INTRODUCTION

Vanadate compounds are observed to form in a variety of crystalline structures, where the coordination of the vanadium by oxygen can be octahedral, square pyramidal, trigonal bipyramidal, or tetrahedral.[1] Correlating with this structural variety, these compounds can be metals, insulators, ferroelectrics, ferromagnets, and potentially multiferroics.[2] The wide range of bonding behavior and associated physical properties can be attributed, in part, to vanadium having three different oxidation states (3+, 4+, and 5+) as well as to vanadium's ability to form strong directional bonds with oxygen. The oxovanadium(IV) ion, VO^{2+}, where V is in the 4+ oxidation state, is one of the most stable biatomic ions known,[3] having a vanadyl short double bond characterized by a bond length of approximately 1.60 Å and significant π-bonding.[4] Further, when V is in the 5+ oxidation state, the 3d shells of vanadium are empty but still near enough to 4s and 4p orbitals to allow for the hybridized bonding behavior with oxygen characteristic of many transition metals.[5]

The $PbVO_3$ (PVO) compound has been the subject of recent experimental and computational studies due to its potential for exhibiting magneto-electric coupling. Under pressure[6] and in epitaxially strained thin films,[7,8] PVO has been reported to form in perovskite-derivative structures that are not observed under ambient conditions. These pressure- and strain-stabilized structures are observed to display a weak vanadyl short bond, square-pyramidal vanadium coordination, and super tetragonality. The vanadium ion has been measured to be in the 4+ oxidation state with a single occupied d orbital, thus having potential for multiferroicity.[7] These experimental studies of PVO have been augmented by computational investigations employing density functional theory (DFT) approaches,[2,6,9−11] which have elucidated key features of the electronic structure and reported a giant electric polarization of 1.52 C/m^2.

In contrast to PVO, relatively little attention has been devoted to exploring strain stabilization of perovskite-derivative structures in alternate vanadate compounds. This is perhaps because many of these systems are non-ferroic in their bulk equilibrium phases under ambient conditions. For example, if the Pb cation in PVO is replaced with a divalent alkaline earth metal, observed equilibrium phases include a metallic cubic perovskite structure (e.g., $SrVO_3$) and a nonpolar $GdFeO_3$-type structure (e.g., $CaVO_3$).[12] If Pb in PVO is replaced with a monovalent alkali metal, a nonpolar centrosymmetric clinopyroxene or orthopyroxene structure results (e.g., KVO_3).[13] However, in the same manner that the perovskite-derivative structure of PVO must be externally stabilized through the application of strain, similar structures

Received: April 11, 2018
Revised: August 10, 2018
Published: August 10, 2018

DOI: 10.1021/acs.chemmater.8b01499
Chem. Mater. 2018, 30, 5870−5877

could form and exhibit ferroic properties for other vanadate systems under yet unexplored epitaxial strain conditions.

In the present study, we employ DFT-based approaches in a computational investigation of the atomic and electronic structure and energetic and polar properties of KVO_3 and $NaVO_3$ perovskite-derivative compounds under biaxial epitaxial strain. We further compare the atomic and electronic properties of these compounds with those computed for the experimentally observed strain-stabilized structure of PVO. For KVO_3, it is shown that a perovskite-derivative structure with space group *Cm* is energetically stabilized under levels of compressive biaxial strains that could be achievable in thin-film growth experiments. For $NaVO_3$, a perovskite-derivative structure with space group *Cm* is shown to be energetically stabilized under levels of tensile biaxial strains also achievable in growth experiments. Similar to PVO, both of the biaxial-strain-stabilized perovskite-derivative compounds of KVO_3 and $NaVO_3$ exhibit large electric polarizations, considerable off-centering of the *B*-site sublattice, and formation of short V−O bonds, which are denoted in this work as vanadyl bonds for these compounds with nominally pentavalent vanadium based on the conventions in ref 1. In contrast with PVO, these compounds do not form a magnetic moment at the *B*-site and produce significantly less displacement of the *A*-site sublattice. The results of this study suggest that strain-stabilized polar perovskite-derivative vanadate compounds may occur for other compositions in addition to PVO and that changes in the *A*-site species can be used to tune the strength of vanadyl bonding and electronic properties in these systems. Control over these properties could be crucial to enabling ferroelectric switching and tuning the magnitudes of polar response properties.

In the remainder of this paper, the computational methods are described in Section 2, and detailed descriptions of the experimentally observed crystal structures of KVO_3, $NaVO_3$, and PVO are given in Section 3. The calculated epitaxial phase diagrams for KVO_3 and $NaVO_3$ are presented in Section 4, with associated electronic structure results discussed in Section 5. The main conclusions are summarized in Section 6.

2. COMPUTATIONAL METHODS

This work examines the effect of biaxial strain on the properties of perovskite-derivative structures of KVO_3 and $NaVO_3$. Here, the term perovskite-derivative structure denotes those that can be derived from the ideal 5-atom cubic perovskite unit cell by imposing biaxial strain in the (001) plane and allowing for tetragonal and monoclinic strains normal to this plane, with arbitrary zone-centered displacements of the *A*- and *B*-site cations and oxygen anions. Such symmetries are meant to mimic those that would be obtained in an epitaxial thin film grown on a substrate with 4-fold symmetry. Examples of such structures are described in Section 4 below.

2.1. Computational Procedure. Construction of the epitaxial phase diagrams was performed using the workflow described in ref 14, which involves a random structure search being conducted at each misfit strain. Specifically, for a given misfit strain, multiple candidates are initialized starting from a cubic perovskite structure and imposing random atomic displacements, leading to unit cells with *P*1 space group symmetry. These candidate structures are subsequently structurally relaxed in DFT calculations, holding the in-plane lattice parameters constant. The lowest-energy structure resulting from these optimizations is selected at each misfit strain and used to generate a ground-state epitaxial phase diagram. A similar approach is used for the experimentally observed 80-atom KVO_3 *Pbcm* structure. For this compound, candidate structures at each misfit strain are generated from the experimental *Pbcm* structure biaxially strained to be coherent with a 4-fold substrate at a given lattice constant and imposing random atomic displacements to again reduce the space group symmetry to *P*1.

Energies of all relaxed structures are referenced to that of the compounds observed under ambient conditions, as discussed in Section 3. The experimental structures are subjected to multiple DFT relaxations prior to use as energy references. Electric polarizations are calculated for epitaxial structures at each misfit strain considered, and electronic structures are computed for the minimum energy epitaxial structures of KVO_3 and $NaVO_3$, as well as the perovskite-derivative PVO structure discussed in Section 3 for purposes of comparison.

2.2. Calculation Details. All DFT calculations made use of the Vienna ab initio simulation package (VASP)[15−18] version 5.4.1. A conjugate-gradient algorithm was used for all structural relaxations. As the standard VASP software package does not allow for arbitrary mechanical boundary conditions, relaxations performed under fixed in-plane strain used a custom-modified version of the VASP software in which components of the stress tensor can be fixed at zero. All relaxations of structures were continued until the forces and out-of-plane stresses converged to magnitudes within 0.001 eV/Å and 0.005 eV/f.u., respectively, where eV/f.u. is per five-atom formula unit.

Calculations used the Ceperley-Alder form of the local density approximation (LDA) exchange-correlation functional, as parametrized by Perdew and Zunger,[19] with the electron−ion interaction described by the projector augmented wave method.[20,21] The LDA is employed because it tends to produce more accurate structural parameters in perovskite oxides, whereas generalized gradient approximation (GGA)-based methods can greatly overestimate the c/a ratios in these systems.[22] Use of the LDA in the present work does lead to well-known systematic errors in the calculated lattice constants, resulting in an underestimation of their values of approximately one percent.[23,24]

A 600 eV plane-wave cutoff energy and the tetrahedron smearing method with Blöchl corrections[25] were used. For calculations of perovskite-derivative structures based on five-atom unit cells, the Brillouin zone was sampled with a 6 × 6 × 6 Monkhorst−Pack[26] grid. In calculations for the 80-atom *Pbcm* epitaxial KVO_3 structure, a 2 × 2 × 6 Monkhorst−Pack sampling was employed. On the basis of tests using different plane-wave cutoffs and k-point meshes, the resulting level of convergence in energy differences using the parameters described above is estimated to be within 0.5 meV/f.u.

Hessian matrices were calculated using Density Functional Perturbation Theory (DFPT)[27] at the gamma point of 2 × 2 × 2 supercells. The Berry-phase approach, as described in the modern theory of polarization,[28] was used to calculate the electric polarization vector of the ground-state phases at each misfit strain. All calculations assume a fixed (vanishing) external electric field corresponding to thin films surrounded by perfectly charge-compensating electrodes, as discussed in refs 29 and 30.

Density of states calculations made use of a more refined k-point grid of 12 × 12 × 12, a 600 eV plane-wave cutoff energy, and the HSE06 hybrid functional.[31] These calculations were performed on the LDA-relaxed structures without reoptimizing the crystal structure with the hybrid functional. The HSE06 functional leads to more accurate electronic structures relative to LDA, with bandgaps agreeing to within 20% of experimentally measured values for transition-metal oxides, as discussed in ref 32.

3. EXPERIMENTALLY OBSERVED CRYSTAL STRUCTURES

Figure 1a,b illustrates the experimentally observed crystal structures for the KVO_3 and $NaVO_3$ compounds that form under ambient conditions.[35,36] For comparison, Figure 1c shows the structure of the PVO phase observed under high-pressure conditions.[6] Table 1 gives the reference lattice constants, Goldschmidt tolerance factors, and space groups for these three structures. Note that the reference lattice constants, a_0, correspond to those of cubic ideal perovskite

DOI: 10.1021/acs.chemmater.8b01499
Chem. Mater. 2018, 30, 5870−5877

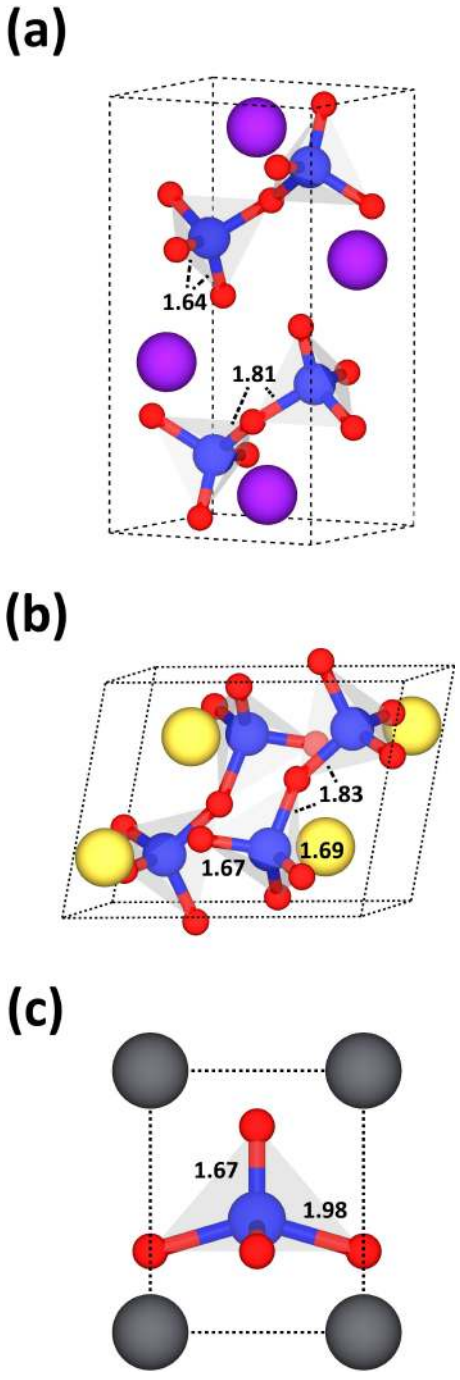

Figure 1. Experimentally observed crystal structures of (a) KVO_3, (b) $NaVO_3$, and (c) PVO. Lengths of unique bonds are indicated in units of Ångstroms. References for structural data are given in the fourth column of Table 1. The PVO phase is observed under pressure or epitaxial strain, while the KVO and NVO phases are observed under ambient conditions. These figures were created using VESTA.[33]

structures, calculated in the same manner as in ref 14. These lattice constants merely form a consistent set of references and have no direct relation to those for the structures shown in Figure 1. For a full description of the structures in Figure 1, see the crystallographic files included as Supporting Information Files 1, 2, and 3. The ionic radii used for calculating tolerance factors are based on the bond valence model.[37] For KVO_3 and $NaVO_3$, all reported energies are referenced to the corresponding calculated DFT energies after relaxation for

Table 1. Properties of the Vanadate Crystal Structures Illustrated in Figure 1[a]

formula	a_0 (Å)	tolerance factor t	space group
KVO_3	3.75	1.153	*Pbcm*[35]
$NaVO_3$	3.68	1.028	*C*2/*c*[36]
$PbVO_3$	3.80	1.015	*P*4*mm*[6]

[a]The second, third, and fourth columns list cubic reference lattice constants, Goldschmidt tolerance factors,[34] and space groups. The references for the data presented in this table are given in the fourth column.

the observed compounds illustrated in Figure 1a,b. Space group symmetries of calculated phases are determined using the Spglib software package.[38] The symmetry precision tolerance value used to assign all space group symmetries (and consequently determine points of phase transition) is 0.01 Å.

The crystal structure of KVO_3 shown in Figure 1a has an orthopyroxene structure with orthorhombic space group *Pbcm*, while the structure of $NaVO_3$ shown in Figure 1b has the clinopyroxene structure with monoclinic space group *C*2/*c*.[13,39] Both structures are centrosymmetric and are characterized by long chains of tetrahedrally coordinated V^{5+} sites extending along a single direction ($^{[2+2]}V^{5+}-_{eq}O_{eq}-^{[2+2]}V^{5+}$ in the notation of ref 1). The vanadium atoms have two terminating *cis* vanadyl bonds, both of length 1.64 Å for KVO_3 and of lengths 1.67 and 1.69 Å for $NaVO_3$, as well as two bridging equatorial bonds, both of length 1.81 Å for KVO_3 and 1.83 Å for $NaVO_3$. Previous experiments have demonstrated that these pyroxene structures can have strongly anisotropic mechanical responses due to their directional bonding along the chain directions.[39]

The orthopyroxene structure of KVO_3 is potentially well-suited to epitaxial growth on a substrate with a surface displaying 4-fold symmetry due to the nearly square arrangement of *A*-sites in the (100) plane. This arrangement is illustrated in the 80-atom supercell representation shown in Figure 2. From this perspective, the vanadium tetrahedra can be seen occupying the centers of slightly distorted cubes formed by *A*-sites.

For comparison, we also consider the pressure-stabilized crystal structure of PVO illustrated in Figure 1c. This is similar to the strain-stabilized PVO structure obtained in thin-film growth experiments.[7] It has the noncentrosymmetric space group *P*4*mm*, exhibits a very large tetragonality (c/a = 1.23), and is accompanied by significant off-centering of both the Pb and V sites.[9] These shifts in ionic positions result in an O_5 pyramid structure coordinating the V atom, with one apical oxygen, O(1), forming a short V−O vanadyl bond with a length of 1.67 Å. The square plane of equatorial O(2) atoms results in four equatorial V−O bonds, all of length 1.98 Å. The large downward displacement of the apical oxygen below the V site leads to a long V−O bond of 3.00 Å, resulting in a two-dimensional layering of corner-shared square pyramids rather than a three-dimensional framework of VO_6 octahedra.[6] The weak interaction between these neighboring layers is likely the reason PVO is not observed to form under ambient conditions. Due to the presence of the lone pair in Pb, the *A*-site is shifted from the center of an 8-fold-coordinated site toward a square O_2 plane, and four of the eight Pb−O(2) distances become much shorter, with lengths of 2.39 Å.[6] The large displacements

DOI: 10.1021/acs.chemmater.8b01499
Chem. Mater. 2018, 30, 5870−5877

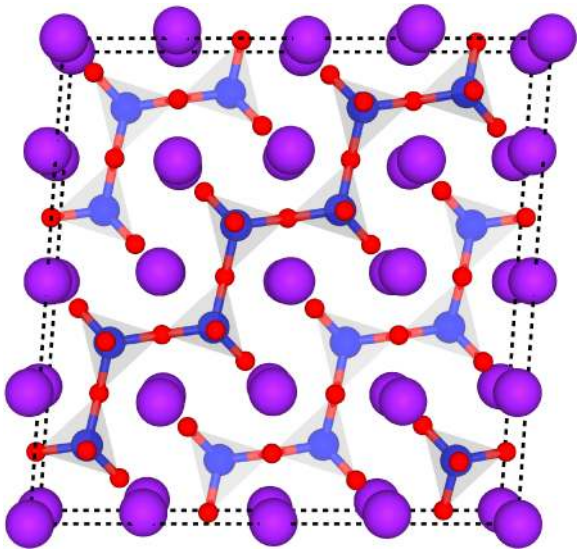

Figure 2. Supercell representation of *Pbcm* KVO_3 (rendered in perspective) illustrating the nearly square symmetry of the *A*-site cations in the (100) plane of the crystal structure shown in Figure 1a. This figure was created using VESTA.[33]

of the sites in PVO lead to a giant electric polarization of 1.52 C/m^2.[10]

4. EPITAXIAL PHASE DIAGRAMS

Figure 3a,b plots the calculated epitaxial phase diagrams for KVO_3 and $NaVO_3$, respectively. Energy is plotted versus misfit strain in the upper panel, while the values for the magnitude (dashed line) and out-of-plane (blue diamonds) and in-plane (red squares and green triangles) components of the electric polarization are plotted in the bottom panel. The horizontal scale on top gives the lattice constant a of a cubic substrate corresponding to the given value of misfit: $a = a_0(\overline{\eta} + 1)$, where a_0 is the compound's reference cubic lattice constant, as listed in Table 1. Energies for each compound are referenced to the DFT-optimized energies of the experimentally observed crystal structures described in Section 3 and can be interpreted as the strain energy of the epitaxially constrained phase, with more positive energies corresponding to larger driving forces for strain relaxation.

Figure 3a plots the energy and polarization versus misfit strain for two epitaxial phases of KVO_3, the perovskite-derivative *Cm* phase (black circles), and the strained derivative of the experimentally observed ambient *Pbcm* phase (red diamonds). As the *Pbcm* phase is paraelectric at all misfit strains, only the *Cm* phase polarization is plotted in the bottom panel.

The energy curve of the KVO_3 *Cm* phase shows stabilization under large compressive misfit strains, with a minimum located at $\overline{\eta} = -3.75\%$ (there is an additional local energy minimum not shown in Figure 3a occurring at $\overline{\eta} = 11.5\%$ with an energy that is 58 meV above that of the reference structure). The corresponding ground-state perovskite-derivative structure at this misfit strain is shown in Figure 4a. This structure is monoclinic ($\beta = 88.9°$), has a very large tetragonal distortion ($c/a = 1.32$), and is 52 meV/f.u. higher in energy than the experimentally observed structure at ambient conditions. Vanadium forms a short vanadyl bond of length 1.64 Å with an apical oxygen, two equatorial bonds of length 1.96 Å with two surrounding oxygens in the square plane, and two

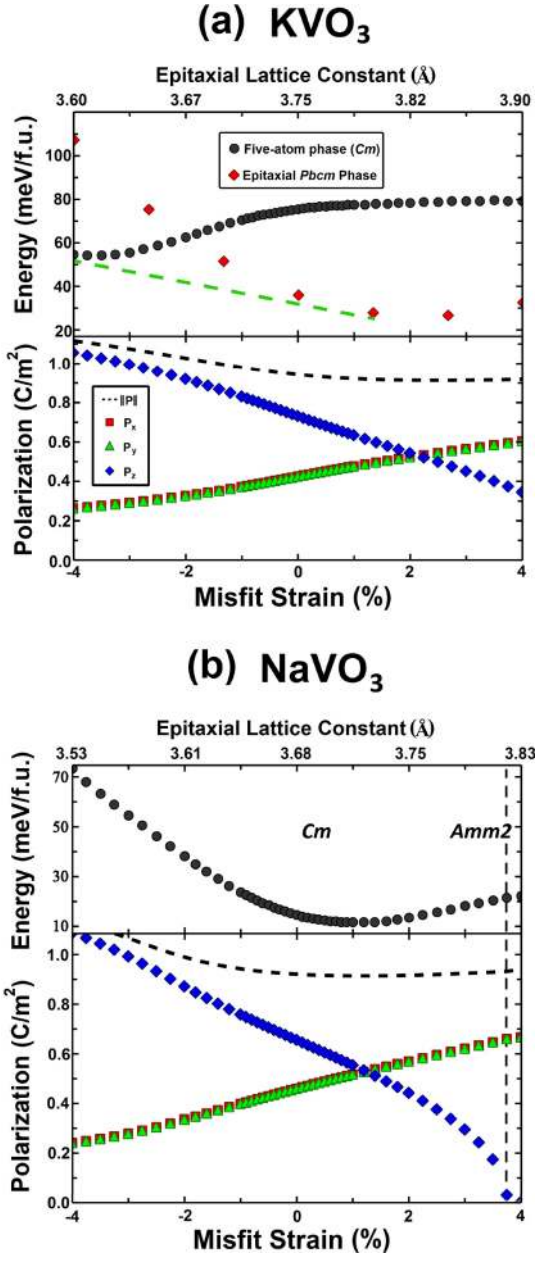

Figure 3. Energies and polarizations plotted against misfit strain for (a) the *Cm* and *Pbcm* phases of KVO_3 and (b) the *Cm* phase of $NaVO_3$. Energies are referenced to the bulk equilibrium phases mentioned in Section 3. The dashed green line in part (a) indicates the common tangent construction for strain-induced phase separation. For the polarizations, out-of-plane (*Pz*) and in-plane (*Px* and *Py*) components, as well as the magnitudes of the total polarization vector, are plotted.

equatorial bonds of length 1.75 Å with the other two oxygens in the plane. The length of the bond between vanadium and the oxygen *trans* to the vanadyl bond is 3.12 Å, leading to a layered square pyramidal arrangement similar to that seen in PVO, but with the 4-fold symmetry along the *c* axis broken by a vanadium displacement along the ⟨111⟩ direction. Analysis of the force-constant matrix for a 2 × 2 × 2 supercell shows that this structure is stable with respect to displacement modes at the zone-center and Brillouin-zone boundaries. The softest eigen-displacement mode has an eigenvalue of 0.45 $eV/Å^2$ (0.15 meV or 1.23 cm^{-1}), supporting the possibility that the

DOI: 10.1021/acs.chemmater.8b01499
Chem. Mater. 2018, 30, 5870−5877

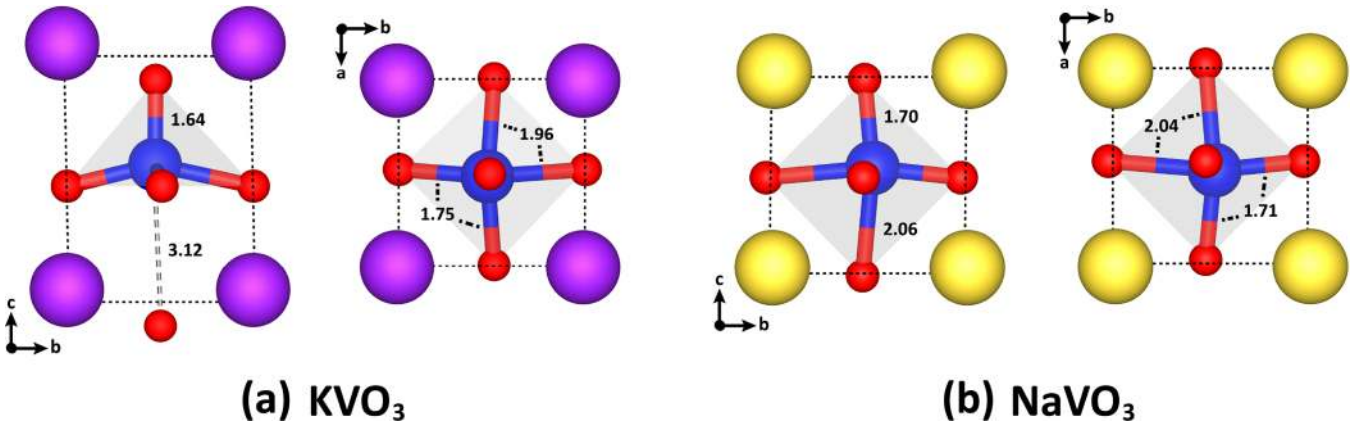

Figure 4. Calculated minimum-energy epitaxial structures of (a) KVO_3 at $\overline{\eta}$ = −3.75% and (b) $NaVO_3$ at $\overline{\eta}$ = 1%. Bond lengths are indicated in units of Ångstroms. This figure was created using VESTA.[33]

minimum energy epitaxial KVO_3 *Cm* phase is stable to non-zone-centered displacement modes that can suppress polarization.[40]

The polarization plot for the *Cm* phase of KVO_3 is shown in the bottom panel of Figure 3a. This plot exhibits smoothly increasing out-of-plane polarization with increasing compressive misfit strain and smoothly increasing in-plane polarization with increasing tensile misfit strain. At the energy minimum ($\overline{\eta}$ = −3.75%), the *Cm* phase has a calculated polarization magnitude of almost 1.1 C/m^2, with the P_z component dominant.

Because of the amenability of the *Pbcm* structure of KVO_3 to (001)-oriented growth on a substrate surface with square symmetry, as described in Section 3, epitaxial calculations of KVO_3 were also performed on a constrained form of this structure, in which in-plane (100) shear was removed in order to simulate lattice matching with the substrate. The energy curve of the epitaxial KVO_3 *Pbcm* phase in Figure 3a has a parabolic shape centered around a minimum epitaxial lattice constant of approximately 3.82 Å. Relative to the *Cm* phase, the *Pbcm* phase is stable under tensile and modest compressive epitaxial strain. However, at nearly −2% misfit strain, there is a crossing of the energy curves, and the *Cm* phase is predicted to be energetically more stable at increasingly compressive misfit strains. A common tangent line can be constructed (dashed green line) between the energy curves of the *Cm* and *Pbcm* phases, which gives the energies of two-phase mixtures[41] between structures with misfit strains of approximately −4% and 1.5%. Following ref 41, this result establishes a bulk energetic driving force for epitaxial films grown in this range of substrate lattice constants to phase separate into two phases, a nonpolar tetrahedrally coordinated *Pbcm* phase with an in-plane lattice constant of around 3.80 Å and a polar square-planar-coordinated *Cm* phase with an in-plane lattice constant of around 3.60 Å. The polar properties of such two-phase films could be of technological interest, as an out-of-plane electric field could drive growth of one or the other phase and potentially elicit a large dielectric response by altering the balance of the phase competition.

To assess whether this phase-separated state can be realized experimentally, the present calculations should be extended in future work to incorporate finite-temperature entropic contributions and account for possible domain structures and interfacial energy effects. Considering the effect of interface energy, it is likely that, for a substrate with square surface symmetry, the contribution would further stabilize the *Cm* phase relative to *Pbcm*. This is because, in the above calculations, the *Cm* phase has an exactly square arrangement of *A*-sites, while the *Pbcm* phase contains only a nearly square arrangement of *A*-sites. The lack of perfect registry for the other atoms in the plane would be expected to increase the interfacial energy.

Figure 3b plots the energy and polarization versus misfit strain for $NaVO_3$. Due to the absence of known competing polymorphs suitable for (001) epitaxy, only predictions for a five-atom perovskite-derivative structure are shown. Under large tensile strains, an *Amm*2 phase is stable, while at all other misfit strains considered, a *Cm* phase is predicted. $NaVO_3$ under epitaxy is destabilized by compressive epitaxial strains and stabilized at modest tensile strains, with a minimum energy structure located at $\overline{\eta}$ = 1%. The structure corresponding to this energy minimum is shown in Figure 4b. It is characterized by a monoclinic angle of β = 89.4° and c/a = 1.01, and it is only 9 meV/f.u. higher in energy than the experimentally observed polymorph at ambient conditions. All oxygen sites are nearly equivalent, each having a short bond with V of around 1.71 Å and a longer bond with V of 2.04 Å. The structure is approximately cubic, with the V atom shifted along the ⟨111⟩ direction to sit preferentially closer to three of the six coordinating oxygen sites. An analysis of the force-constant matrix for a 2 × 2 × 2 supercell shows that this structure is unstable with respect to both in-phase and out-of-phase octahedral rotational modes at the brillouin-zone boundaries, with the most unstable eigen-displacement mode having an eigenvalue of −0.93 eV/Å^2 (15.56*i* meV or 125.46*i* cm^{-1}). In a thicker film, where these modes are not frozen out due to the constraint of epitaxy, the effect on polarization could be sizable.[42] Note that additional epitaxial calculations were performed for $NaVO_3$ in a *Pbcm* phase similar to that of KVO_3 at various misfit strains. However, this variant of $NaVO_3$ gives energies many hundreds of meV higher than that of the reference structure over the misfit strain range shown in Figure 3b. Further, this structure is dynamically unstable and relaxes to perovskite-derived phases if the atoms are perturbed and symmetry is not constrained.

Similar to behavior seen for the KVO_3 *Cm* phase, the out-of-plane polarization for the epitaxially strained $NaVO_3$ structure smoothly decreases while the in-plane polarization smoothly increases with increasing misfit strain. The out-of-plane polarization eventually disappears at the phase boundary

DOI: 10.1021/acs.chemmater.8b01499
Chem. Mater. 2018, 30, 5870−5877

located at $\overline{\eta}$ = 3.75%. The polarization of the minimum energy structure in $NaVO_3$ has a magnitude of 0.92 C/m^2, with nearly equal contributions from in-plane and out-of-plane components.

5. ELECTRONIC STRUCTURES

Figure 5a–c shows the total and projected electronic density of states (DOS) for the PVO, KVO_3, and $NaVO_3$ structures illustrated in Figures 1c and 4a,b, respectively, calculated by the HSE06 hybrid functional. The top panel (black line) of each figure plots the total DOS, while the other three panels plot the DOS projected onto the s, p, and d orbitals of the various sites. Projected DOS are included for the A-cation (red line, A = Pb, K, or Na), vanadium (blue), apical oxygen (light green), and two symmetry-equivalent equatorial oxygen sites (dark green). A comparison of the electronic structures of these three systems leads to key insights into the role of the *A*-site species in the bonding, as well as the effect of changing the nominal vanadium oxidation state from V^{4+}, as in PVO, to V^{5+}, for KVO_3 and $NaVO_3$. The nominal oxidation state for these latter two systems is assumed on the basis of their d^0 transition element *B*-sites.[1]

Figure 5a plots the DOS for the PVO structure shown in Figure 1c. The electronic structure of PVO has been calculated previously[2,6,9] using semilocal DFT, while the present work employs hybrid functionals. With the exception of the band gap, the present results are very similar to those reported in previous work, and thus a discussion of the PVO DOS will be limited here. It should be noted that, in prior work, a *C*-type antiferromagnetic ordering of the magnetic moments has been shown to be slightly lower in energy than a ferromagnetic (FM) ordering.[6] In the present work, which is focused on exploring trends across the different vanadate compounds, we have considered only the FM state, which yields a magnetic moment of 1 μ_B/f.u., localized on the V ion. The PVO DOS in Figure 5a features a bandgap of 2.35 eV determined by the splitting between occupied and unoccupied V 3d states. A single electron occupies the majority-spin vanadium d_{xy} state (blue, −1 to 0 eV), resulting in vanadium having a V^{4+} (d^1) configuration in an ionic picture. We note that, in the DOS calculations for the PVO compound, we neglected the effects of spin–orbit coupling (SOC), which can be expected to be relatively large for the heavy Pb ion. On the basis of previous calculations where these effects were considered for Pb-based perovskite oxides,[43] the features of the DOS near the valence and conduction band edges are not expected to be significantly altered.

The stereochemically active Pb site plays an important role in the bonding and electronic structure of PVO. Both the Pb–O and V–O bonds display covalent character. As shown in Figure 5a, the Pb 6s states in the valence band and low-lying Pb 6p states in the conduction band mix with O 2p states. These same O 2p states also display hybridization with V 3d states, thus suggesting competition between vanadyl and Pb–O bonds; this effect is discussed in detail in ref 2. As a result of this competition, the vanadyl bond in PVO is relatively weak, as evidenced by a relatively long bond length compared to vanadyl bonds commonly observed in inorganic compounds.

Figure 5b,c shows DOS plots for the minimum energy epitaxial phases (see Figure 4) of KVO_3 and $NaVO_3$, respectively. Both are charge-transfer insulators with the states at the valence-band maximum (VBM) being largely of O 2p character. The HSE06 bandgaps of KVO_3 and $NaVO_3$ are 2.07

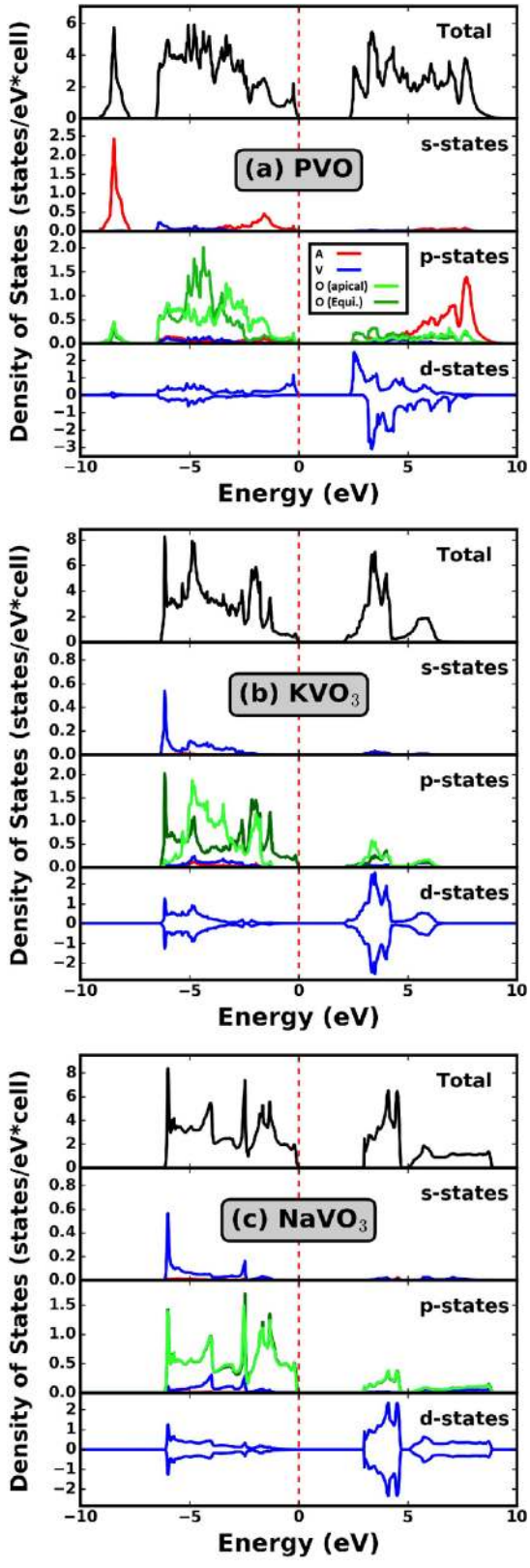

Figure 5. Total and projected density of states for (a) PVO (Figure 1c), (b) KVO_3 (Figure 4a), and (c) $NaVO_3$ (Figure 4b). Black lines indicate values of the total DOS, while colored lines give values of the projected DOS, with values of the A-cation in red, vanadium in blue, the apical oxygen in light green, and the two symmetry-equivalent equatorial oxygens in dark green. For d states, spin-up and spin-down states are denoted by positive and negative values. The zero of energy in the horizontal axis is set to the Fermi level.

DOI: 10.1021/acs.chemmater.8b01499
Chem. Mater. 2018, 30, 5870–5877

and 2.98 eV, respectively. The ground state is non-spin-polarized in both structures. Both in the valence and conduction bands, the V 3d states of KVO_3 and $NaVO_3$ mix significantly with O 2p states, indicating strong covalent character. In general, the strong tetragonal distortion of KVO_3 results in distinct electronic behaviors for the apical versus the equatorial O sites, whereas the almost cubic lattice in $NaVO_3$ leads to nearly identical behavior for all of the O sites. Unlike PVO, no *A*-site states appear near the VBM. At approximately 6.5 eV below the VBM, both systems exhibit a sharp peak corresponding to states with mixed V 4s, O 2p, and V 3d character. In the case of KVO_3, the equatorial O 2p states mix with largely V s and V $3d_{x^2-y^2}$ states, while in $NaVO_3$, both the apical and equatorial O states mix with V 4s and equal parts V $3d_{z^2}$ and V $3d_{x^2-y^2}$ states. The states above approximately −5 eV are largely of V $3d_{xz}$ and V $3d_{yz}$ character for KVO_3 and equal parts V $3d_{xz}$, V $3d_{yz}$, and V $3d_{xy}$ for $NaVO_3$. The apical O states in KVO_3 mix more strongly with these states in a second peak. The states at the VBM are of dominant O 2p character in both compounds, and those at the conduction-band minimum are of primarily V 3d character.

As mentioned above, the strength of the vanadyl bond in PVO is relatively weakened by the spatially extended Pb 6p electronic states that compete with vanadium in the bonding with oxygen. It thus seems reasonable that substitution of Pb with a cation not possessing these extended 6p states might facilitate vanadyl bonding in the system. When this is examined in ref 2 by DFT calculations, replacement of Pb^{2+} with Ca^{2+} leads to broadening of the t_{2g} bands and alteration of the crystal field so that the vanadyl bond is no longer stabilized. A key result of the calculations shown in Figure 5 is that the strength of the vanadyl bond is strengthened by replacing the divalent Pb *A*-site cation with monovalent Na or K. The monovalent alkali metal *A*-sites do not have the spatially extended 6p states needed to bond covalently with oxygen, and their presence also does not spoil the crystal field scheme required to stabilize strong V−O bonding. The result is significant mixing between occupied V 3d and O 2p states, which is consistent with the shorter average V−O bond lengths of these two systems as compared to those of PVO.

6. SUMMARY

The ground-state epitaxial phases and energetic, polar, and electronic properties of two alkali-metal vanadates, KVO_3 and $NaVO_3$, are studied computationally by DFT calculations. Both KVO_3 and $NaVO_3$ exhibit epitaxially stabilized perovskite-derivative phases with vanadyl bonding, large polarizations, and low epitaxial strain energies. The predicted ground-state epitaxial phase diagram for KVO_3 shows an energetic driving force for strain-induced phase separation between a structure with *Cm* symmetry having a large polarization and square pyramidal coordination of the *B*-site and a nonpolar epitaxial *Pbcm* structure displaying tetrahedral coordination of the *B*-site. The electronic structure of the epitaxial phases of KVO_3 and $NaVO_3$ are calculated and compared with those of the experimentally observed perovskite-derivative PVO compound. These calculations show that substitution of divalent Pb cations with monovalent K or Na increases the strength of the vanadyl bond, due to the removal of the spatially extended Pb 6p states that compete with V−O bonding.

■ ASSOCIATED CONTENT

Supporting Information

The Supporting Information is available free of charge on the ACS Publications website at DOI: 10.1021/acs.chemmater.8b01499.

Crystallographic information file for the minimum energy DFT-relaxed (under epitaxial constraints) *Cm* phase of KVO_3 (CIF)

Crystallographic information file for the minimum energy DFT-relaxed (under epitaxial constraints) *Pbcm* phase of KVO_3 (CIF)

Crystallographic information file for the minimum energy DFT-relaxed (under epitaxial constraints) *Cm* phase of $NaVO_3$(CIF)

■ AUTHOR INFORMATION

Corresponding Author

*E-mail: angsten@berkeley.edu.

ORCID

Thomas Angsten: 0000-0001-8763-5321

Lane W. Martin: 0000-0003-1889-2513

Notes

The authors declare no competing financial interest.

■ ACKNOWLEDGMENTS

This work was supported by the U.S. Department of Energy, Office of Science, Office of Basic Energy Sciences, Materials Sciences and Engineering Division under Contract No. DE-AC02-05-CH11231: Materials Project program KC23MP. T.A. acknowledges a fellowship through the National Science Foundation Graduate Research Fellowship Program (Grant No. DGE1106400).

■ REFERENCES

(1) Schindler, M.; Hawthorne, F. C.; Baur, W. H. Crystal Chemical Aspects of Vanadium: Polyhedral Geometries, Characteristic Bond Valences, and Polymerization of (VO_n) Polyhedra. *Chem. Mater.* **2000**, *12*, 1248−1259.

(2) Singh, D. J. Electronic structure and bond competition in the polar magnet $PbVO_3$. *Phys. Rev. B: Condens. Matter Mater. Phys.* **2006**, *73*, 094102.

(3) Selbin, J. The Chemistry of Oxovanadium(IV). *Chem. Rev.* **1965**, *65*, 153−175.

(4) Ballhausen, C. J.; Gray, H. B. The Electronic Structure of the Vanadyl Ion. *Inorg. Chem.* **1962**, *1*, 111−122.

(5) Evans, H. T., Jr. Refinement and vanadium bonding in the metavanadates KVO_3, and KVO_3-H_2O Crystal. *Z. Kristallogr.* **1960**, *114*, 257−277.

(6) Shpanchenko, R. V.; Chernaya, V. V.; Tsirlin, A. A.; Chizhov, P. S.; et al. Synthesis, Structure, and Properties of New Perovskite $PbVO_3$. *Chem. Mater.* **2004**, *16*, 3267−3273.

(7) Martin, L. W.; Zhan, Q.; Suzuki, Y.; Ramesh, R.; Chi, M.; Browning, N.; Mizoguchi, T.; Kreisel, J. Growth and structure of $PbVO_3$ thin films. *Appl. Phys. Lett.* **2007**, *90*, 062903.

(8) Oh, S.; Shin, H.-Y.; Yoon, S.; Ahn, J.; Cha, J.; Hong, S.; Kang, S.; Kim, M.; Choi, S.; Roh, C.; Lee, J.; Jo, W. Strain-induced non-linear optical characteristics of pyroelectric $PbVO_3$ epitaxial thin films. *Opt. Mater. Express* **2017**, *7*, 62−72.

(9) Uratani, Y.; Shishidou, T.; Ishii, F.; Oguchi, T. First-principles predictions of giant electric polarization. *Jpn. J. Appl. Phys.* **2005**, *44*, 7130−7133.

(10) Uratani, Y.; Shishidou, T.; Oguchi, T. First-principles study on the magnetic anisotropy in multiferroic $PbVO_3$ and $BiCoO_3$. *J. Phys. Soc. Jpn.* **2009**, *78*, 084709.

DOI: 10.1021/acs.chemmater.8b01499
Chem. Mater. 2018, 30, 5870−5877

(11) Ming, X.; Hu, F.; Du, F.; Wei, Y. J.; Chen, G. First-principles study of multiferroic material $PbVO_3$ under uniaxial pressure. *Eur. Phys. J. B* **2015**, *88*, 212.
(12) Chamberland, B. L.; Danielson, P. S. First-principles study on the magnetic anisotropy in multiferroic $PbVO_3$ and $BiCoO_3$. *J. Solid State Chem.* **1971**, *3*, 243.
(13) de Waal, D.; Heyns, A. M. Vibrational spectra of $NaVO_3$, KVO_3 and the solid solutions $(Na_{0.88}K_{0.12})VO_3$ and $(Na_{0.5}K_{0.5})VO_3$. *Mater. Res. Bull.* **1992**, *27*, 129−136.
(14) Angsten, T.; Martin, L.; Asta, M. Orientation-dependent properties of epitaxially strained perovskite oxide thin films: Insights from first-principles calculations. *Phys. Rev. B: Condens. Matter Mater. Phys.* **2017**, *95*, 174110.
(15) Kresse, G.; Hafner, J. Ab initio molecular dynamics for liquid metals. *Phys. Rev. B: Condens. Matter Mater. Phys.* **1993**, *47*, 558−561.
(16) Kresse, G.; Hafner, J. Ab initio molecular-dynamics simulation of the liquid-metalamorphous-semiconductor transition in germanium. *Phys. Rev. B: Condens. Matter Mater. Phys.* **1994**, *49*, 14251−14269.
(17) Kresse, G.; Furthmüller, J. Efficient iterative schemes for ab initio total-energy calculations using a plane-wave basis set. *Phys. Rev. B: Condens. Matter Mater. Phys.* **1996**, *54*, 11169−11186.
(18) Kresse, G.; Furthmüller, J. Efficiency of ab-initio total energy calculations for metals and semiconductors using a plane-wave basis set. *Comput. Mater. Sci.* **1996**, *6*, 15−50.
(19) Perdew, J. P.; Zunger, A. Self-interaction correction to density-functional approximations for many-electron systems. *Phys. Rev. B: Condens. Matter Mater. Phys.* **1981**, *23*, 5048−5079.
(20) Blöchl, P. E. Projector augmented-wave method. *Phys. Rev. B: Condens. Matter Mater. Phys.* **1994**, *50*, 17953−17979.
(21) Kresse, G.; Joubert, D. From Ultrasoft Pseudopotentials to the Projector Augmented Wave Method. *Phys. Rev. B: Condens. Matter Mater. Phys.* **1999**, *59*, 1758−1775.
(22) Bilc, D. I.; Orlando, R.; Shaltaf, R.; Rignanese, G. M.; Íñiguez, J.; Ghosez, P. Hybrid exchange-correlation functional for accurate prediction of the electronic and structural properties of ferroelectric oxides. *Phys. Rev. B: Condens. Matter Mater. Phys.* **2008**, *77*, 165107.
(23) Diéguez, O.; Rabe, K. M.; Vanderbilt, D. First-principles study of epitaxial strain in perovskites. *Phys. Rev. B: Condens. Matter Mater. Phys.* **2005**, *72*, 144101.
(24) Dawber, M.; Rabe, K. M.; Scott, J. F. Physics of thin-film ferroelectric oxides. *Rev. Mod. Phys.* **2005**, *77*, 1083−1130.
(25) Blöchl, P. E.; Jepsen, O.; Andersen, O. K. Improved tetrahedron method for Brillouin-zone integrations. *Phys. Rev. B: Condens. Matter Mater. Phys.* **1994**, *49*, 16223−16233.
(26) Monkhorst, H.; Pack, J. Special points for Brillouin zone integrations. *Phys. Rev. B* **1976**, *13*, 5188−5192.
(27) Baroni, S.; et al. Green's-Function Approach to Linear Response in Solids. *Phys. Rev. Lett.* **1987**, *58*, 1861−1864.
(28) Resta, R.; Vanderbilt, D. Theory of polarization: A modern approach. *Top. Appl. Phys.* **2007**, *105*, 31−68.
(29) Kolpak, A. M.; Sai, N.; Rappe, A. M. Short-circuit boundary conditions in ferroelectric thin films. *Phys. Rev. B: Condens. Matter Mater. Phys.* **2006**, *74*, 054112.
(30) Indlekofer, K. M.; Kohlstedt, H. Simulation of quantum dead-layers in nanoscale ferroelectric tunnel junctions. *Europhys. Lett.* **2005**, *72*, 282.
(31) Krukau, A. V.; Vydrov, O. A.; Izmaylov, A. F.; Scuseria, G. E. Influence of the exchange screening parameter on the performance of screened hybrid functionals. *J. Chem. Phys.* **2006**, *125*, 224106.
(32) Garza, A. J.; Scuseria, G. E. Predicting Band Gaps with Hybrid Density Functionals. *J. Phys. Chem. Lett.* **2016**, *7*, 4165−4170.
(33) Momma, K.; Izumi, F. VESTA 3 for three-dimensional visualization of crystal, volumetric and morphology data. *J. Appl. Crystallogr.* **2011**, *44*, 1272−1276.
(34) Goldschmidt, V. M. Die Gesetze der Krystallochemie. *Naturwissenschaften* **1926**, *14*, 477−485.
(35) Hawthorne, F. C.; Calvo, C. The crystal chemistry of the M^+VO_3 pyroxenes. *J. Solid State Chem.* **1977**, *22*, 157−170.
(36) Marumo, F.; Isobe, M.; Iwai, S.; Kondō, Y. α-Form of sodium metavanadate. *Acta Crystallogr., Sect. B: Struct. Crystallogr. Cryst. Chem.* **1974**, *30*, 1628−1630.
(37) Brown, I. D. Bond valences-a simple structural model for inorganic chemistry. *Chem. Soc. Rev.* **1978**, *7*, 359.
(38) Atztogo.github.io/spglib/.
(39) Adams, D. M.; Christy, A. G.; Haines, J.; et al. The phase stability of the alkali-metal vanadates at high pressures studied by synchrotron X-ray powder diffraction and infrared spectroscopy. *J. Phys.: Condens. Matter* **1991**, *3*, 6135−6144.
(40) Benedek, N. A.; Fennie, C. J. Why are there so few perovskite ferroelectrics? *J. Phys. Chem. C* **2013**, *117*, 13339−13349.
(41) Xue, F.; Li, Y.; Gu, Y.; Zhang, J.; Chen, L. Q. Strain phase separation: Formation of ferroelastic domain structures. *Phys. Rev. B: Condens. Matter Mater. Phys.* **2016**, *94*, 220101.
(42) Angsten, T.; Asta, M. Epitaxial phase diagrams of $SrTiO_3$, $CaTiO_3$, and $SrHfO_3$: Computational investigation including the role of antiferrodistortive and A-site displacement modes. *Phys. Rev. B: Condens. Matter Mater. Phys.* **2018**, *97*, 134103.
(43) Gierlich, A. *All-Electron GW Calculations for Perovskite Transition-Metal Oxides*. Ph.D. thesis, RWTH Aachen University, Bonn, Deutschland, 2011.

DOI: 10.1021/acs.chemmater.8b01499
Chem. Mater. 2018, 30, 5870−5877